

Discerning ground state and photoemission-induced spin textures in altermagnetic α -MnTe

D.A. Usanov*,^{1,2} S.W. D'Souza*,³ A. Dal Din*,⁴ J. Krempaský,² F. Guo,¹
O.J. Amin,⁴ C. Polley,⁵ M. Leandersson,⁵ G. Carbone,⁵ B. Thiagarajan,⁵
T. Jungwirth,^{6,4} L. Šmejkal,^{7,8,9} J. Minár,³ P. Wadley,⁴ and J.H. Dil^{1,2}

¹*Institut de Physique, École Polytechnique Fédérale
de Lausanne, CH-1015 Lausanne, Switzerland*

²*Center for Photon Science, Paul Scherrer Institut, CH-5232 Villigen, Switzerland*

³*University of West Bohemia, New Technologies
Research Center, Plzen 30100, Czech Republic*

⁴*School of Physics and Astronomy, University of Nottingham,
Nottingham NG7 2RD, United Kingdom*

⁵*MAX IV Laboratory, Lund University, 221 00 Lund, Sweden*

⁶*Institute of Physics, Czech Academy of Sciences,
Cukrovarnická 10, 162 00 Praha 6 Czech Republic*

⁷*Max Planck Institute for the Physics of Complex Systems, 01187 Dresden, Germany*

⁸*Max Planck Institute for Chemical Physics of Solids, 01187 Dresden, Germany*

⁹*Institute of Physics, Czech Academy of Sciences,
Cukrovarnická 10, 162 00 Praha 6 Czech Republic*

(Dated: March 18, 2026)

Abstract

Recently discovered altermagnets provide a physical realization of an unconventional compensated magnetic phases with a higher partial-wave type of ordering, reminiscent of unconventional superfluid phases. Their stability under normal conditions has sparked significant research interest, spanning fields from spintronics to topological and correlated quantum materials. Spin- and angle-resolved photoemission spectroscopy (SARPES) has great promise to resolve the momentum-dependent spin textures intricately interweaved with the altermagnetic real space spin order. Using the relativistic d -wave-like spin polarization on one of the nodal surfaces of the altermagnetic band structure of α -MnTe as an example, we here identify and resolve the challenges associated with (S)ARPES studies on altermagnets and offer insights into data interpretation. We focus particularly on the role of photoemission-induced electron polarization and the coupling between light and the Néel vector of a magnetic domain. Our findings reveal an extraordinary behaviour of photoemission selection rules while using linearly-polarized light. We observe, and distinguish, polarization of photoelectrons originating from the sample's ground state spin texture, on one hand, and from the photoemission process, on the other hand. Our experimental results are supported by a combination of ab initio band-structure and 1-step photoemission calculations.

Keywords: altermagnetism, MnTe, ARPES, matrix element effects, 1-step photoemission calculations, spin-resolved ARPES, d-wave

I. INTRODUCTION

Altermagnetism is a recently identified magnetic phase characterized by a compensated collinear order that breaks spin degeneracy in the electronic band structure. The unconventional nature of the altermagnetic ordering stems from the spontaneously broken spin-space and real-space rotation symmetries, while preserving a symmetry combining the spin-space and real-space rotation transformations [1, 2]. Unlike ferromagnetic ordering with s -wave-like spin polarization in the band structure generating net magnetization, and unlike conventional antiferromagnetic ordering with spin-degenerate bands, the compensated altermagnetic ordering features a distinctive d -wave (g or i -wave) spin polarization of the band structure. [1, 2].

Since their theoretical conception, altermagnetic phases have been predicted in a wide

variety of material classes, including insulators, semiconductors, semimetals, metals, and superconductors [2, 3]. Among these candidates, manganese telluride (MnTe) stands out as a prototypical system that has attracted growing theoretical and experimental interest [1, 2, 4]. MnTe crystallizes in three main structural forms: zinc blende, wurtzite, and nickeline [5, 6]. The nickeline (NiAs-type) phase, known as α -MnTe [7–14], is the focus of the present study. α -MnTe is a semiconductor with an indirect band gap of approximately $E_g \approx 1.27\text{--}1.46$ eV [15], and it belongs to the hexagonal space group $P6_3/mmc$. Its magnetic structure consists of two Mn sublattices, A and B , aligned antiparallel with respect to each other with a Néel temperature of 310 K [16]. These sublattices are connected by a non-symmorphic sixfold screw-axis along the c -axis, but are not related by simple translation or inversion [1, 7, 17]. This symmetry-breaking arrangement gives rise to an electronic structure with g -wave spin splitting, characterized by three nodal planes Γ -K-A. The fourth nodal plane Γ -K-M (referred later as $k_z = 0$) arises from a mirror symmetry connecting the opposite-spin sublattices. This non-relativistic spin splitting has been previously referred as ‘strong’ altermagnetic lifted Kramer’s spin degeneracy (LKSD) and discussed elsewhere [7].

As the next step, spin degeneracy within the nodal planes can be lifted by the spin-orbit coupling (SOC) in altermagnets without breaking the crystal inversion symmetry. In particular, within the $k_z = 0$ nodal plane, the resulting spin polarization (S_z) is perpendicular to the axis of the manganese magnetic moments in the direct crystal space. This unconventional out-of-plane polarization component has a d -wave-like spin symmetry (Fig. 1). There are two Γ -K_{*i*}(-M_{*i*}) paths showing the same spin splitting and one with a larger splitting and inverted polarization. The orientation of this d -wave-like spin splitting of the iso-energy surface is dictated by the Néel vector, which has 6 possible orientations (at low temperature) along one of the easy axes (corresponding to the $\Gamma - M_i$ directions in the momentum space). This mechanism is called ‘weak’ altermagnetic LKSD [7] and is the main focus of this paper.

This unconventional d -wave-like out-of-plane spin texture can be accessed via different experimental techniques. Apart from x-ray magnetic circular dichroism (XMCD) [4, 18–22] and anomalous Hall effect measurements [17, 23], spin- and angle-resolved photoemission (SARPES) [7, 24–27] is able to provide the most direct access to the band structure polarization of solids. However, the angular distribution of photoelectrons is always affected by matrix element effects [28], which should be taken into account. Moreover, the complexity of ARPES data interpretation increases greatly when adding spin resolution, since electron

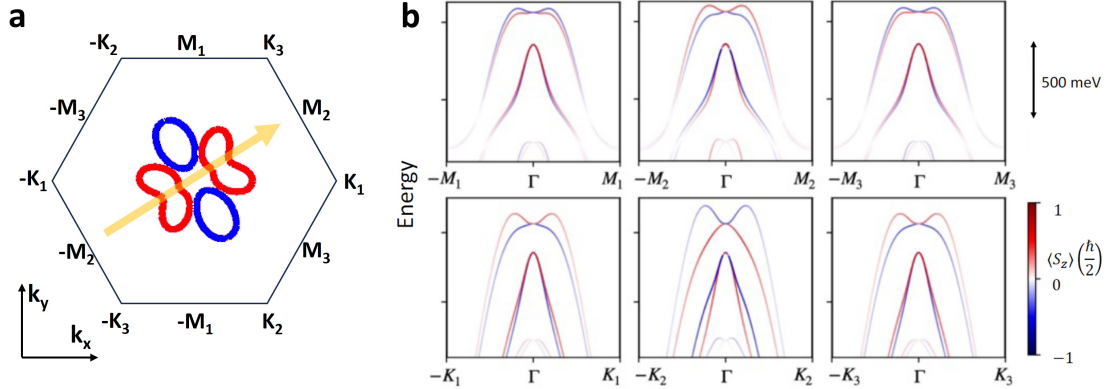


FIG. 1. (a) Schematic representation of 2D d -wave-like out-of-plane polarization symmetry in the reciprocal space. Notation of high-symmetry points of the Brillouin zone at $k_z = 0$ is shown. d -wave symmetry of S_z is sketched on the Fermi surface cut at binding energy -0.1 eV. The Néel vector is indicated with a yellow arrow. (b) shows the spin-polarized band structure along the $\bar{\Gamma} - \bar{K}_i$, $\bar{\Gamma} - \bar{M}_i$ paths at $k_z = 0$ [7].

polarization is also largely affected by the light polarization, experimental geometry and final states of photoemission. Matrix element effects are known to be able not only to alter polarization amplitude, but they may also completely change the observed spin texture with respect to the ground state [29–32]. That is why it is essential to decouple signals arising from the ground state and from the photoemission process.

This study aims to provide insights into challenges associated with (S)ARPES measurements of antiferromagnetic MnTe and data interpretation. We focus on the electronic bands close to the Fermi level and around the nodal plane $k_z = 0$ accessed from (0001) surface of MnTe and consider only out-of-plane spin polarization S_z .

II. RESULTS AND DISCUSSIONS

A. 1-step simulation of photoemission from MnTe

As discussed above, the band structure of a single magnetic domain in MnTe exhibits an out-of-plane spin texture of the d -wave-like symmetry around the $k_z = 0$ nodal plane. Both the sign and the orientation of this texture are determined by the in-plane Néel vector. However, in an (S)ARPES experiment, this ground-state spin texture is significantly influenced

by matrix element effects of the photoemission process. These effects depend not only on the photon energy but also on the relative orientation of the sample, light polarization, and the general experimental geometry. In altermagnetic materials such as MnTe, the orientation of the Néel vector plays a particularly critical role. To illustrate this, let us consider one-step photoemission calculations at the $k_z = 0$ nodal plane using a photon energy of $h\nu \approx 80$ eV (see Fig. 2 and Fig. 8 in SI). In these calculations, polarization of photoelectrons are computed for fixed experimental conditions, varying only the Néel vector orientation and/or the light polarization.

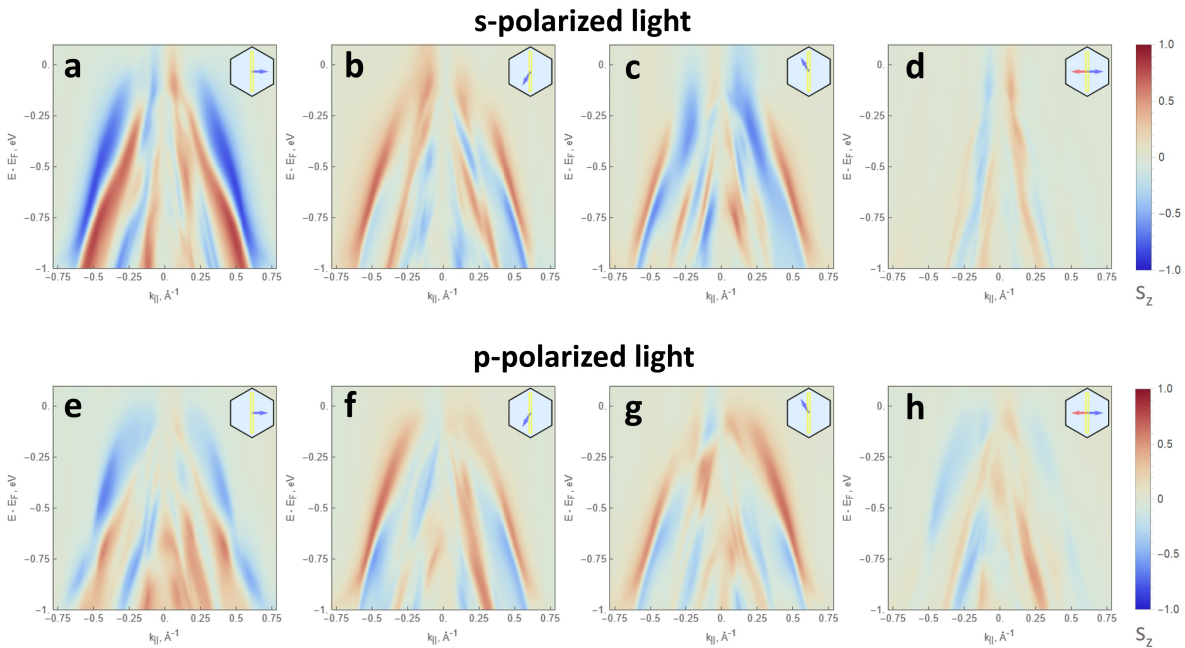


FIG. 2. Calculated SARPES maps of the out-of-plane spin polarization at the $k_z = 0$ nodal plane at $h\nu = 82$ eV along $\bar{K} - \bar{\Gamma} - \bar{K}$ direction. The domain orientation and experimental geometry in each plot are sketched in the inset. (a)-(d) correspond to the s -polarized light, (e)-(h) correspond to p -polarized light.

Across all configurations, the calculated spin polarization of the photocurrent reveals a structure more complex than that of the ground state. Specifically, the modulation of the out-of-plane spin component S_z strongly depends on the orientation of the Néel vector relative to the ARPES measurement geometry. Furthermore, this modulation varies significantly when changing light polarization (Fig. 2(e-h)). A similar dependence is observed in the spin-integrated photoemission intensity (see Fig. 6 in SI), underscoring the critical role

of matrix element effects in interpreting (S)ARPES data.

It is important to note that photoelectrons can possess non-zero spin polarization even if the ground state has effectively zero net polarization everywhere in the Brillouin zone. To illustrate this, we simulated photoemission from a sample consisting of two magnetic domains with opposite Néel vectors (Fig. 2(d) and (h)). Since flipping of the Néel vector results in spin-reversal in the entire band structure, the averaged ground-state polarization of such a sample becomes zero everywhere in the Brillouin zone. However, the resulting photocurrent polarization is non-zero, with features symmetric and antisymmetric with respect to the Γ point and with a strong dependence on the light polarization.

The influence of matrix element effects on spin polarization for all orientations of Néel domains is detailed in Section VI B in the SI. For the experimental geometry used in the presented (S)ARPES measurements, the use of *s*-polarized (LV) light adds a photoemission-induced spin signal, which is purely antisymmetric with respect to the Γ point. In contrast, under *p*-polarized (LH) light, symmetric components emerge as well. Additionally, we identify a region in the Brillouin zone — defined by $k_{\parallel} > 0.25$ and $E_B < 0.5$ eV — where the impact of matrix element effects is minimal. This region-of-interest (ROI) is therefore well suited for probing the intrinsic spin texture of the ground state and has been predominantly used in our SARPES measurements (reported also in [27]).

Based on the one-step calculations, we propose a simple rule for interpreting out-of-plane spin polarization signals around the $k_z = 0$ nodal plane in SARPES experiments on MnTe. Any S_z spin polarization component that is antisymmetric with respect to the Γ point originates exclusively from matrix element effects. In contrast, symmetric components may reflect the symmetry of both the ground-state spin texture and matrix element contributions. In the special case of *s*-polarized light, the symmetric part of the spin signal reflects the ground-state properties.

B. Influence of multiple domains

(S)ARPES measurements of real α -MnTe samples are, in fact, even more complex than the 1-step predictions described above. It is associated with the fact that the characteristic size of a magnetic domain in MnTe thin films is of the order of $0.1 \mu\text{m}$ in the absence of patterning [4]. Therefore, any conventional synchrotron-based ARPES experiment will most

likely probe simultaneously several domains with different orientation.

There are 6 possible Néel vector orientations - along each Γ - M_i direction. The band structure of domains with the opposite Néel vector are spin-flipped with respect to each other. Therefore, we can define two basic scenarios of possible domain configurations under the photon beam: either the overall domain composition is balanced or there is a preponderance of a certain Néel direction. The first case is logically assumed for a non-field-cooled sample, where the total net spin polarization in the ground state averages out to zero everywhere in the Brillouin zone. We will discuss the balanced case first, and will focus on imbalanced domain configurations afterwards.

1. *Balanced domain configuration*

We have performed ARPES measurements on non-field-cooled samples in the VUV range with and without spin resolution. First, photon energy, and thus k_z scans in the range between $h\nu = 19$ to 82 eV were measured in order to locate the $k_z = 0$ nodal planes. In this region of reciprocal space, the relativistic spin splitting does not risk to be overshadowed by its non-relativistic counterpart, which may also contain non-altermagnetic contributions [33]. In Fig. 3 constant energy slices through the specified photon energy range are displayed at binding energies of 150 and 500 meV. From the observed periodicity, and comparison to *ab-initio* calculations and already published data [8, 10, 14, 34, 35], several $k_z = 0$ planes can be located. For our further investigation we choose the one around $h\nu = 78$ eV because of the clean spectral weight and the large signal to noise ratio over a large binding energy range. Importantly, in this photon energy range we mainly observe bands dispersing in k_z , thus indicating their bulk origin. At the same time, we do not exclude a presence of a surface resonance (Fig. 3a) close to the zone center at around $k_{||} < \pm 0.2 \text{\AA}^{-1}$.

In Figure 4 we plot constant energy surfaces 100 meV below the valence band maximum and the band dispersion along the $\bar{K} - \bar{\Gamma} - \bar{K}$ direction for different light polarizations near the $k_z = 0$ nodal planes at $h\nu = 78$ and $h\nu = 21$ eV. Similar to previous works [7–10], a clear band splitting on the order of 100 meV can be observed along the $\bar{\Gamma} - \bar{K}$ direction. Along $\bar{\Gamma} - \bar{M}$ the splitting is smaller and hence more difficult to resolve (Fig. 1).

Both linear and circular dichroism are clearly visible in the constant energy surfaces. Because the latter is antisymmetric with regard to the scattering plane (which coincides

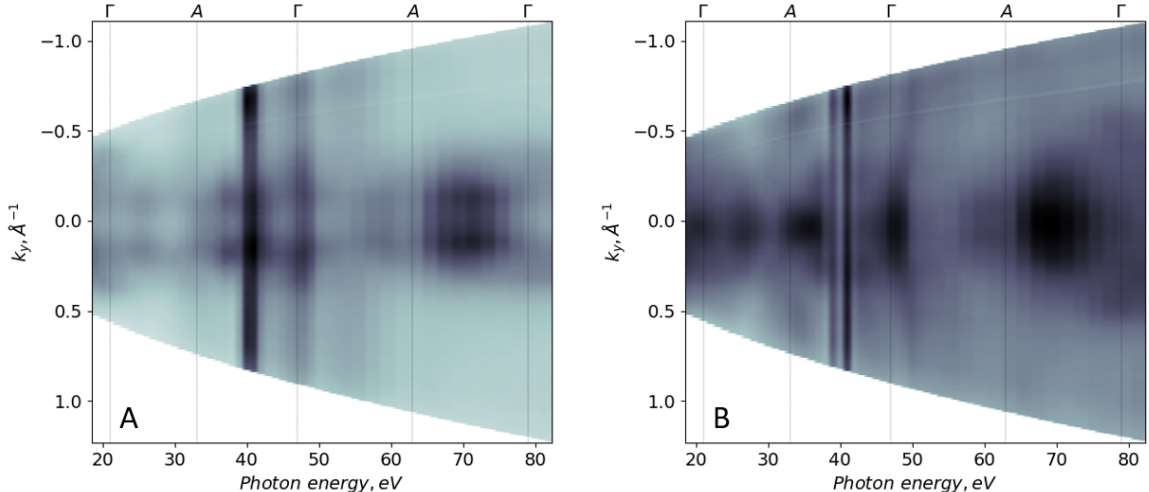


FIG. 3. Constant energy slices (100 meV integration) from the photon energy scan at (a) $E_B = 150$ meV and (b) $E_B = 500$ meV measured with p -polarized light along $\bar{K} - \bar{\Gamma} - \bar{K}$ direction. Positions of high symmetry points are indicated. Constant-angle intense lines at $h\nu \approx 40$ and 48 eV are instrumental artifacts due to high order harmonics coming from the undulator.

with a mirror plane), we ascribe it to an effect of the experimental geometry [36] (Fig. 9(a) in SI). Noteworthy, the iso-energy cuts obtained by summing both circular polarizations (see Fig. 9(b) in SI) are close to 6-fold symmetric. Because we do not observe 2-fold signatures of a single domain, it does not seem possible to deduct the exact domain configuration. The reason is the finite energy, k_z and angular resolution of the ARPES experiment compared to the difference in spin splitting between nonequivalent high-symmetry directions. Therefore, it suggests that spin-integrated ARPES is much less sensitive to the domain orientation than spin-resolved ARPES.

At the same time, the linear dichroism and the corresponding spectral weight distribution (Fig. 4(a-b)) can not be explained solely by standard dipole selection rules [28]. The angular distribution of photoelectrons observed with p -polarized light does not contradict the dipole selection rules of photoemission from p_z orbitals (since these Te bands near E_F have the dominant p -orbital component along the c -axis [7]). However, s -polarized light should result in an intensity minimum within the scattering plane (for all p and d orbital components), which is exactly the opposite with respect to our experimental observation. Apart from a violation of dipole selection rules and the plane-wave final state picture of photoemission, we hypothesize a selective photoexcitation of different Néel domains by linearly-polarized

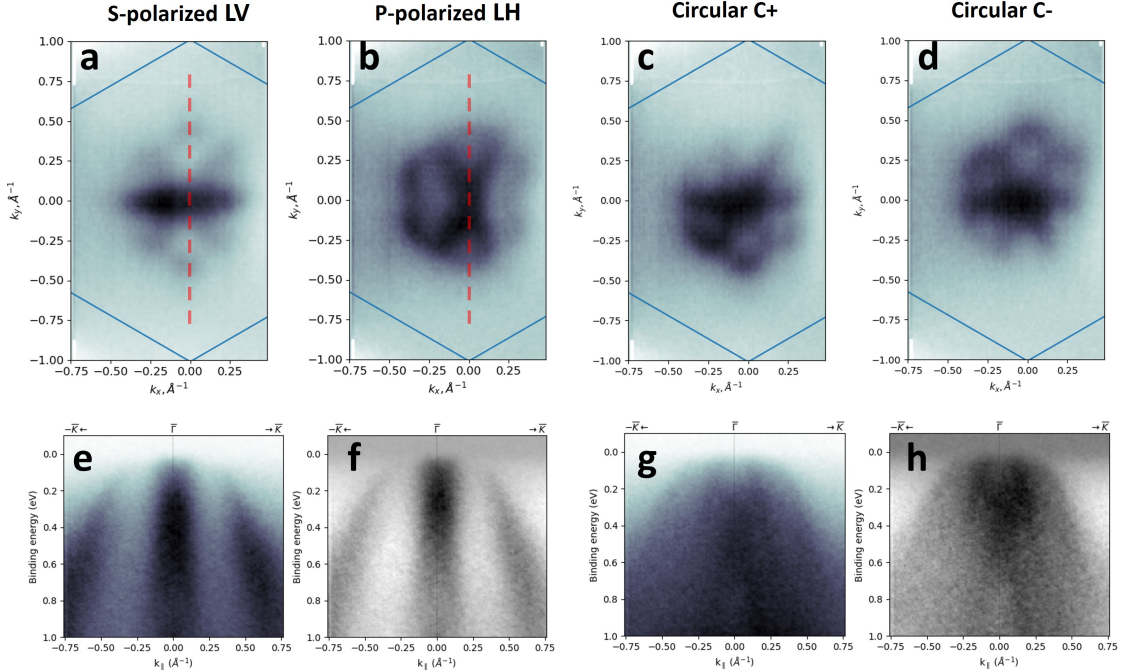


FIG. 4. (a)-(d) Constant energy maps 100 meV below E_F for 4 different light polarizations, taken with $h\nu = 78$ eV, the borders of the surface Brillouin zone are indicated; (e)-(h) corresponding bandmap cuts along the $\bar{K} - \bar{\Gamma} - \bar{K}$ directions, indicated with dashed red lines in (a) and (b); (e) and (g) show the raw data, (f) and (h) display the data with angle-integrated background subtracted for better visibility.

light. Spectral weight is enhanced within the scattering plane, when \vec{E} is perpendicular to it, emphasizing mostly domains with the Néel vector perpendicular to \vec{E} . As will be explained below, this selectivity also affects the observed spin polarization of photoelectrons.

In Figure 5(a) we present the calculated spin signal along $\bar{K} - \bar{\Gamma} - \bar{K}$ for the configuration with six equally contributing domains. Contrary from what would be expected from the ground state spin texture, a clear antisymmetric spin signal is present close to the zone center. As discussed above, this spin polarization originates purely from the selection rules of the photoemission process and is also visible close to the Fermi level in the experimental SARPES data obtained for small in-plane momenta ($k_{\parallel} \approx 0.2 \text{ \AA}^{-1}$). For larger momenta, the spin signal is expected to be practically zero in this case of a balanced domain configuration, which is related to the spin-compensated polarization of the ground state.

2. Imbalanced domain configuration

In order to get access to ground-state-related spin polarization, an imbalance in the domain population should be created. In our case, we employed so-called field cooling - cooling down the sample from a paramagnetic state in presence of static out-of-plane magnetic field [4]. In this section we will present the results obtained from a field-cooled thin film.

In an experiment on thin films, which have not undergone any micromanufacturing, we do not expect to get a single domain after the field cooling. Instead, we expect to induce an imbalance only between opposite Néel domains [4]. In Figure 5(b-d) such an imbalance is simulated for a domain configuration sketched in the inset and has the following composition: Ground state 1 (blue arrows) = (24; 19; 19)%, Ground state 2 (red arrows) = (10; 14; 14)%, corresponding to an average domain imbalance (effective "magnetization") of 0.28. Besides the antisymmetric spin signal close to Γ , now a clear symmetric spin texture, originating from the ground state, is expected at higher momenta. This is exactly what has been observed experimentally in a SARPES measurement of the field-cooled sample. Spin-resolved energy-distribution curves (EDC) at $k_{\parallel} \approx 0.36 \text{ \AA}^{-1}$ show a clear symmetric spin signal, resembling the EDCs extracted from the calculations. Spin-resolved EDCs at higher momenta possess the same symmetry (see Fig. 10 in SI). Since the impact of the matrix element effect has been predicted to be minimal in this region of the Brillouin zone (Fig. 8), the observed polarization signal reflects mostly the ground-state spin texture. Therefore, these data support the concept of the SOC-induced lifted Kramers spin degeneracy in altermagnetic MnTe.

Based of the 1-step photoemission calculations, we summarize the effect of domain orientation on the measured spin polarization of photoelectrons excited by linearly-polarized light (a more detailed description is available in [37]). Let us first consider the $\bar{K} - \bar{\Gamma} - \bar{K}$ direction perpendicular to the light scattering plane and utilizing *s*-polarized light (Fig. 5(b)). Our analysis of the 1-step photoemission calculations shows that mainly the domains with the Néel vector parallel to the scattering plane define the polarization texture in the ROI; all other domains provide smaller photoelectron current. Consequently, the polarization signal in this region of the Brillouin zone mainly reflects an imbalance between two domains of opposite Néel vectors perpendicular to \vec{E} (Fig. 2(d)). Spin-resolved EDCs are predicted to

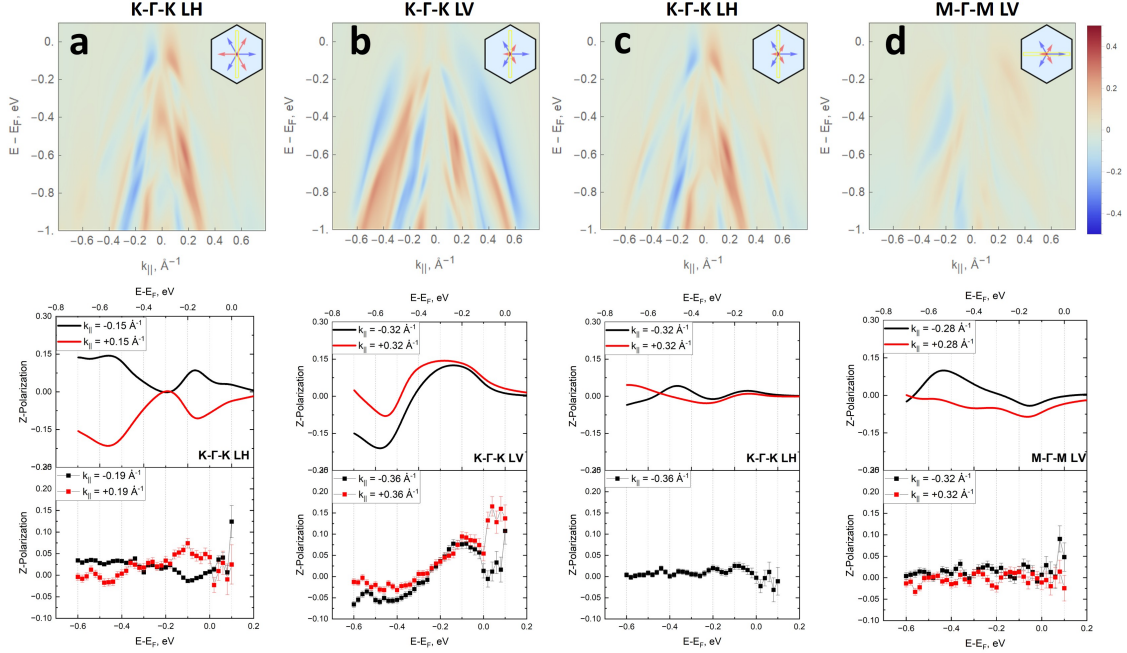


FIG. 5. SARPES 1-step calculations and measurements for the balanced (a) an imbalanced (b)-(d) domain configurations. The measured data were taken at $h\nu = 78$ eV and the calculated ones are at $h\nu = 82$ eV. The experimental geometry and domain combinations are shown in the inset.

be symmetric with respect to the Γ point with a small impact of antisymmetric features. This was indeed observed in the experiment (Fig. 5(b) and Fig. 10 in SI). Moreover, even for a perfect balance of 3 non-equivalent Néel domains of the same ground state, the symmetric character in ROI remains.

A completely different picture is formed by utilizing p -polarized light with the same experimental geometry (Fig. 5(c)). One may notice an almost complete disappearance of features related to the ground state. What remains is mostly anti-symmetric (with respect to the zone center) and has a predominant photoemission origin. Specifically for the ROI, the polarization signal is negligibly small and hence less feasible to detect in a real experiment. This was confirmed by measuring a spin-resolved EDC on one side at $k_{\parallel} = -0.36 \text{ \AA}^{-1}$, where polarization does not exceed a few %.

Regarding the $\bar{M} - \bar{\Gamma} - \bar{M}$ direction, which lies within the scattering plane, and photoemission using s -polarized light (Fig. 5(d)), the domain superposition does not generally lead to a very distinguishable polarization signal as in $\bar{K} - \bar{\Gamma} - \bar{K}$. Even though both symmetric and anti-symmetric spin signals are expected in the ROI, they lack a general trend (in

contrast to $\bar{K} - \bar{\Gamma} - \bar{K}$) and their amplitude is comparable with the detection limit. This model qualitatively reproduces the measured polarization, where no clear spin signal has been detected.

III. CONCLUSIONS

In this work, we presented a (S)ARPES investigation of the spin-orbit-induced spin texture in altermagnetic α -MnTe, addressing both the experimental challenges of spin-resolved photoemission measurements and the complexities inherent in interpreting the resulting data.

(S)ARPES measurements have been performed on (0001) surface of MnTe thin films around the $k_z = 0$ nodal plane at $h\nu = 78$ eV. Linear dichroism effects, that go beyond simple dipole selection rules, suggest a selective excitation of magnetic domains, depending on the orientation of the Néel vector with respect to both the light polarization and the scattering geometry. This coupling between the light polarization and the Néel vector was further corroborated by SARPES measurements on a field-cooled sample: a clear spin polarization signal was observed with s -polarized light, whereas p -polarized light resulted in an effectively unpolarized signal. Supported by 1-step photoemission calculations, the ground-state-related polarization signal has been decoupled from the polarization induced by the photoemission process. In particular, under specific experimental conditions, spin polarization, which is symmetric with respect to the Γ point, is attributed to the ground-state spin texture, whereas antisymmetric polarization originates from the photoemission process. These findings are consistent with a qualitative model involving a superposition of multiple domains, each exhibiting a d -wave-like spin texture.

Our results highlight the intrinsic complexity of SARPES investigations in MnTe and, in general, in altermagnetic materials. First, the band structure with lifted Kramers degeneracy - including both occupied and unoccupied states — introduces significant final-state effects. Second, the interaction of spin-polarized bands with polarized light causes additional modulations of photoelectron current and spin polarization. Third, these effects are further influenced by crystal orientation, the direction of the Néel vector, and the experimental geometry. These considerations have to be taken into account when aiming to assess properties of the initial state spin texture. In combination with symmetry arguments, it en-

hances the feasibility to support the *d*-wave-like concept in MnTe experimentally [27]. The final degree of complexity arises from the presence of multiple magnetic domains within the ARPES probing area. All of these factors must be carefully considered to reliably interpret spin-resolved photoemission data in altermagnetic systems.

IV. METHODS

The α -MnTe thin films were synthesized at the University of Nottingham, with a thickness of 30 nm, grown at 700 K by molecular beam epitaxy (MBE) on InP(111)A substrates with *c*-axis aligned with the surface normal, analogous to [4]. The samples were transferred in a custom-build vacuum suitcase under the UHV conditions to the end-station without breaking the vacuum. In accordance with previous experiments [4], tellurium surface termination is expected. Field cooling has been performed using permanent magnets (0.4 T field) with the magnetic field aligned with (0001) orientation of the films. The samples were first heated to 350 K (above the transition temperature around 310 K), then cooled down to a base temperature of 100 K using liquid nitrogen. P-type doping of the films has been identified [4].

The electronic structure calculations shown in Fig. 1 were performed for bulk MnTe (space group $P6_3/mmc$, No. 194). The lattice parameters were taken from X-ray diffraction measurements [38]. Electronic structure calculations were carried out using the Vienna Ab initio Simulation Package (VASP) [39], employing the Perdew–Burke–Ernzerhof (PBE) functional [40] with spin–orbit coupling enabled and electron correlations treated using the Dudarev-type spherically symmetric Hubbard correction as in Ref. [17]. An $8 \times 8 \times 5$ k-point mesh and an energy cutoff of 520 eV were used.

The spin and angle-resolved photoemission (SARPES) calculations are performed by employing one-step model of photoemission, originally proposed by Pendry and co-workers [41–43], as implemented in the fully relativistic SPR-KKR program package [44, 45]. Within the framework of multiple scattering theory, photocurrent from the Mn-terminated surface of hexagonal MnTe(0001) has been calculated in a direct way by determining the initial and final states for a semi-infinite atomic half-space using the low-energy electron diffraction (LEED) method [46]. The surface potential is described through a spin-dependent Rundgren–Malmström barrier [47]. The On-site Coulomb interaction parameters for Mn 3d states

($U = 4.80\text{eV}$, $J = 0.80\text{eV}$) within LSDA+U were chosen. The final states are calculated as the best available single-particle approach, “time-reversed spin-polarized LEED state”, and initial states are represented by the retarded one-electron Green function in a semi-infinite half-space. The photoemission calculations are performed by taking into consideration the actual measurement ARPES geometry to correctly account for the wave-vector, spin- and energy-dependent transition matrix elements [43, 48, 49] along with all multiple scattering effects in the initial and final states, the effect of the photon momentum vector, and the escape depth of the photoelectrons via an imaginary part in the potential function.

In order to simulate the photoemission current from a particular domain configuration, signal from each domain orientation and for a selected light polarization in the common emission plane are added incoherently. Spin-resolved energy distribution curves in Fig. 5 were extracted from the 1-step calculations taking into account finite energy and k_{\parallel} resolution of the experiment.

Spin-integrated and spin-resolved measurements on MnTe films have been performed at the B-branch of the Bloch beamline [50] in the range of $h\nu = 19\text{-}82$ eV. The beam spot size of the sample is expected to be around $12.5 \mu\text{m} \times 15.5 \mu\text{m}$. For the presented spin-resolved data we used an energy resolution of 57 meV and angular integration of 1.5° along the analyzer slit and 0.5° perpendicular to it, corresponding to approx. 0.1 \AA^{-1} and 0.04 \AA^{-1} at $E_{kin} = 73$ eV respectively. A VLEED (Very Low Energy Electron Diffraction) detector FerrumTM from Focus GmbH was employed as electron polarimeter and is based on the spin-dependent exchange scattering of low energy electrons from a magnetized target (oxidized 10nm-thick Fe film on a W(001) crystal).

In all measurements and calculations, the c-axis of the MnTe crystal structure was perpendicular to the samples’ surface, exposing either a manganese or tellurium layer. All spin-resolved data presented in this paper correspond to the S_z polarization component aligned with the c-axis of the MnTe crystal. The c-axis was aligned with the optical axes of the hemispherical analyzer. The $\bar{K} - \bar{\Gamma} - \bar{K}$ direction was aligned with the HSA entrance slit.

V. ACKNOWLEDGMENTS

D.A.U. acknowledges support from the Swiss National Science Foundation through the Spark grant CRSK-2 228962. F.G. and J.H.D. acknowledge support from the Swiss National Science Foundation (SNSF) Project No. 200021-200362. S.W.D and J.M acknowledge support from the QM4ST project funded by Programme Johannes Amos Comenius, call Excellent Research (Project No. CZ.02.01.01/00/22_008/0004572)

VI. SUPPLEMENTARY INFORMATION

A. Comparison of the experimental and 1-step calculated data

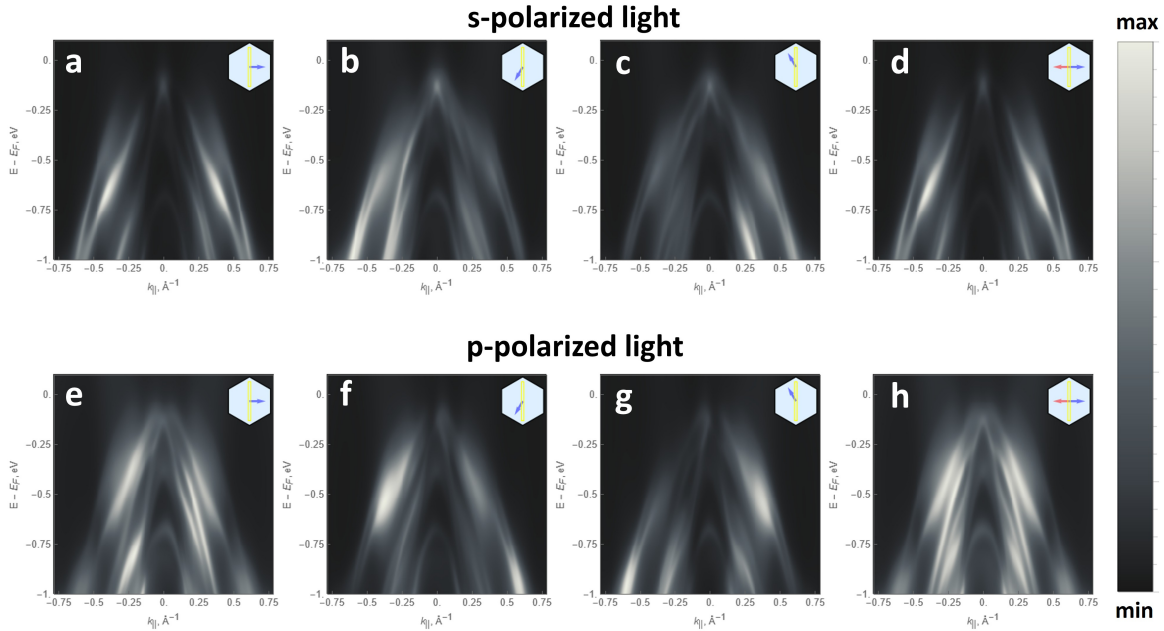


FIG. 6. Same as fig. 2, but displaying spin-integrated photoelectron current: Calculated ARPES bandmaps at the $k_z = 0$ nodal plane at $h\nu = 82$ eV along $\bar{K} - \bar{\Gamma} - \bar{K}$ direction. The domain orientations and experimental geometry in each plot are sketched in the inset. (a)-(d) correspond to the s -polarized light, (e)-(h) correspond to p -polarized light.

Figures 6 and 7 focus on spin-integrated 1-step photoemission calculations and experimental ARPES data. The calculations predict a strong dependence of photoelectron distribution on the Néel vector direction and light polarization. However, due to the finite energy and

angular resolution in the experiment, we were not able to employ this effect to access the domain configuration under the photon beam. Figure 7 displays a comparison between spin-integrated ARPES bandmaps and the ones calculated for a domain combination, where all opposite Néel vectors are equally present and thus spin-compensated. Due to the p-doping of the sample, the calculated bands are shifted by 100 meV compared to those measured by ARPES.

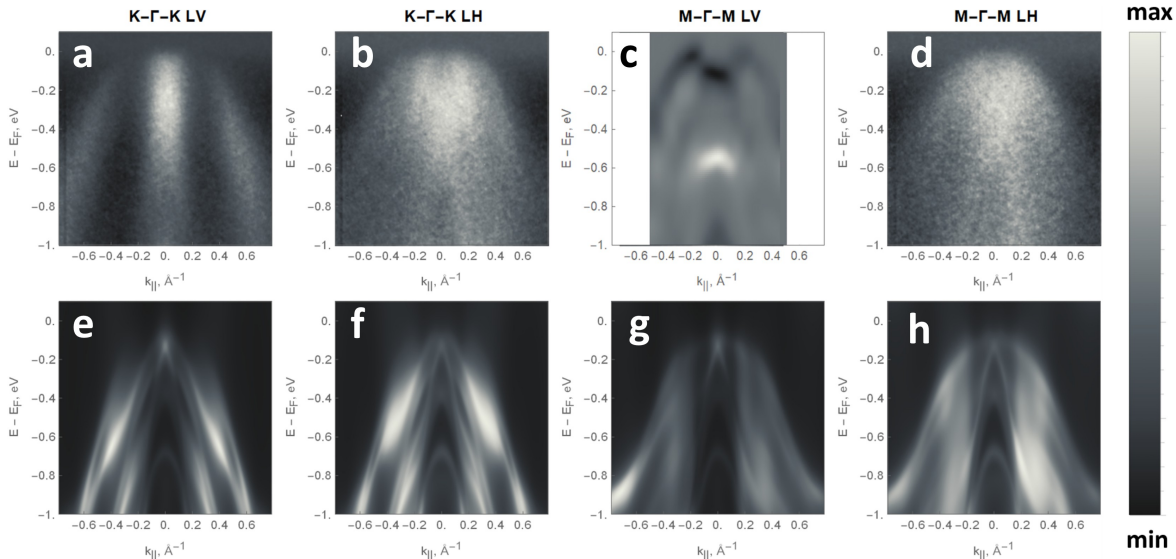


FIG. 7. Measured (a-d) and 1-step calculated (e-h) spin-integrated band maps for the fully-compensated domain configuration. The light polarization and reciprocal space directions are indicated. The experimental data in (a), (b) and (d) is shown with angle-integrated background subtracted, and the data in (c) is displayed as a curvature plot for better visualization.

B. Impact of matrix element effects on spin polarization of photoelectrons

In order to deduce the contribution of the matrix element effects on the observed spin polarization, we performed the following analysis of the present 1-step photoemission calculations. By using the same ground state spectral function, we computed difference in SARPES signal between two opposite incidence angles of the photon beam. This is equivalent to a scenario, when the light incidence is kept constant, but the sample as a whole undergoes azimuthal rotation by 180 degrees. Thus, the difference between these two orientations highlights spectral features, which change sign upon the sample rotation and hence

are attributed only to the effect of geometry in matrix elements of photoemission. The results for $\bar{K} - \bar{\Gamma} - \bar{K}$ and $\bar{M} - \bar{\Gamma} - \bar{M}$ with s - and p -polarized light are displayed in Fig. 8. We emphasize that 180° azimuthal rotation of the sample is not the same as flipping the Néel vector, since the first one does not change the ground-state spin polarization of the band structure, but the second one causes a sign flip of S_z .

The SARPES signal presented below originates from the geometrical contribution of matrix element effects and will be always present on top of features related to the ground-state polarization. Noteworthy, this contribution is purely anti-symmetric with respect to the Γ point for the s -polarized light (LV), when the electric field vector \vec{E} always lies in the sample's surface plane. On the contrary, when \vec{E} has a finite angle with respect to the surface (in our case - 45 degrees), some symmetric part of the photoemission-induced spin signal is also present. In addition, we indicate a minimal impact in the region-of-interest - $k_{\parallel} > 0.25$ and $E_B < 0.5eV$. This region is hence a good choice to access spin textures related to the ground state.

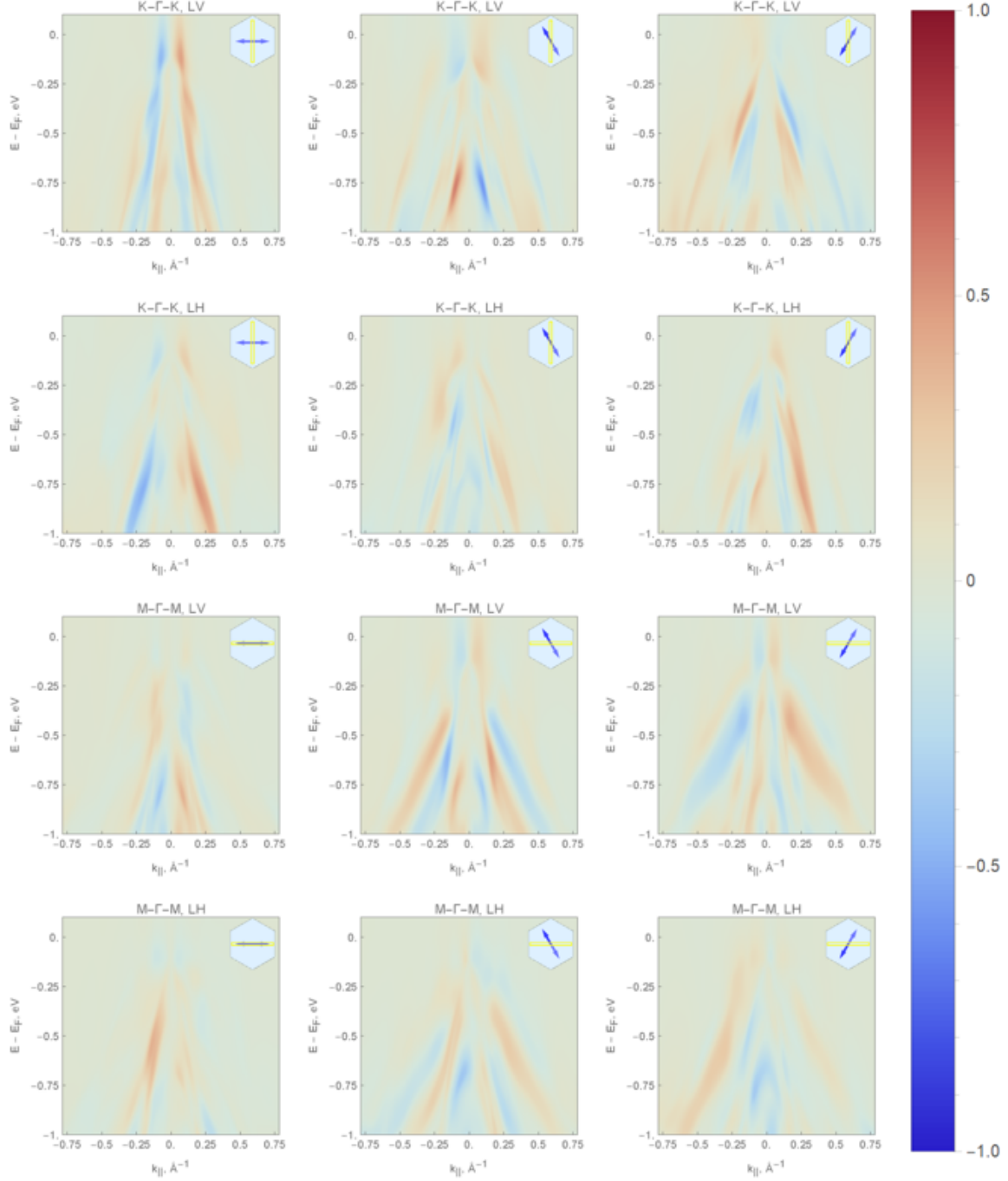


FIG. 8. Bandmaps of spin polarization arising from the photoemission process for differently oriented domains and s - and p - polarized light (LV and LH, respectively).

C. Circular dichroism in ARPES data

In Fig. 9(a) we show constant energy cuts obtained by summing signal from both circular light polarizations from a non-field-cooled sample. So-called circular integrated signal effectively suppress the contribution of matrix element effects in angular distribution of photoelectrons. The angular distribution of the spectral weight shows predominant 6-fold symmetry. Because we do not observe 2-fold signatures of a single domain, it does not seem possible to deduct the exact domain configuration, taking into account finite energy and angular resolution of the ARPES experiment with respect to the spin splitting difference between nonequivalent high-symmetry directions.

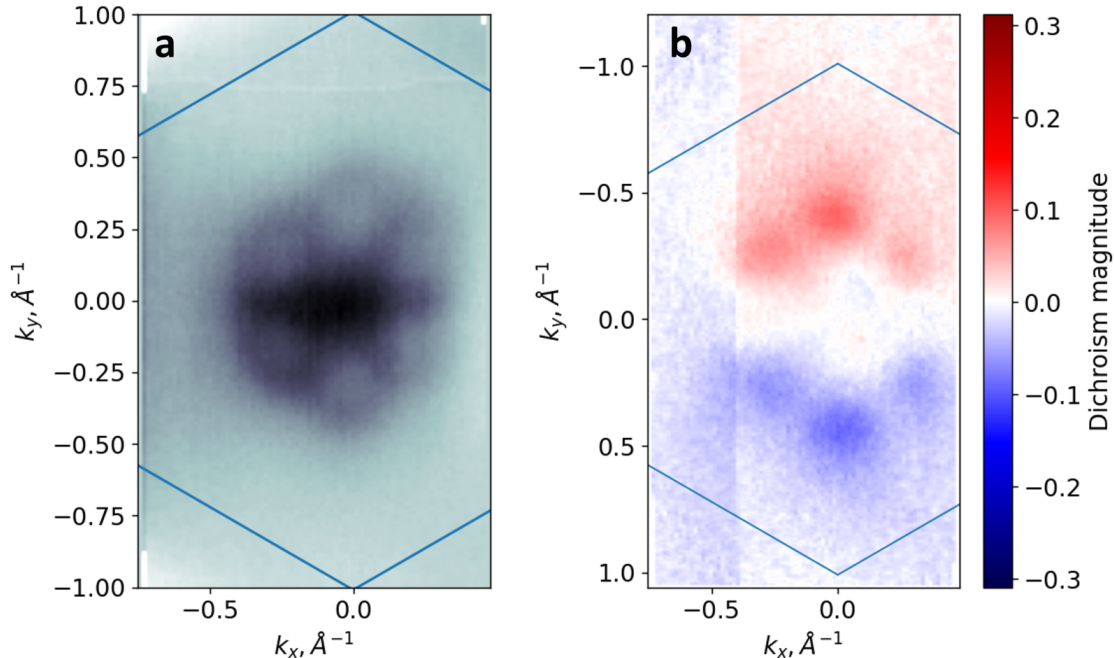


FIG. 9. Constant energy cuts of circular integrated (a) and circular dichroic (b) signal from a non-field-cooled sample.

The observed pattern of circular dichroism in angular distribution of photoelectrons (CDAD) in Fig. 9(b) is antisymmetric with respect to the scattering plane of photoemission (the plane formed by the direction of the incident light and the surface normal). Since it coincides with the mirror plane of the non-magnetic crystal, we fully attribute the observed CDAD to the geometry of the photoemission experiment [36, 51]. Therefore, it suggests that

spin-integrated ARPES is much less sensitive to the domain orientation than spin-resolved ARPES.

D. Supplementary SARPES data

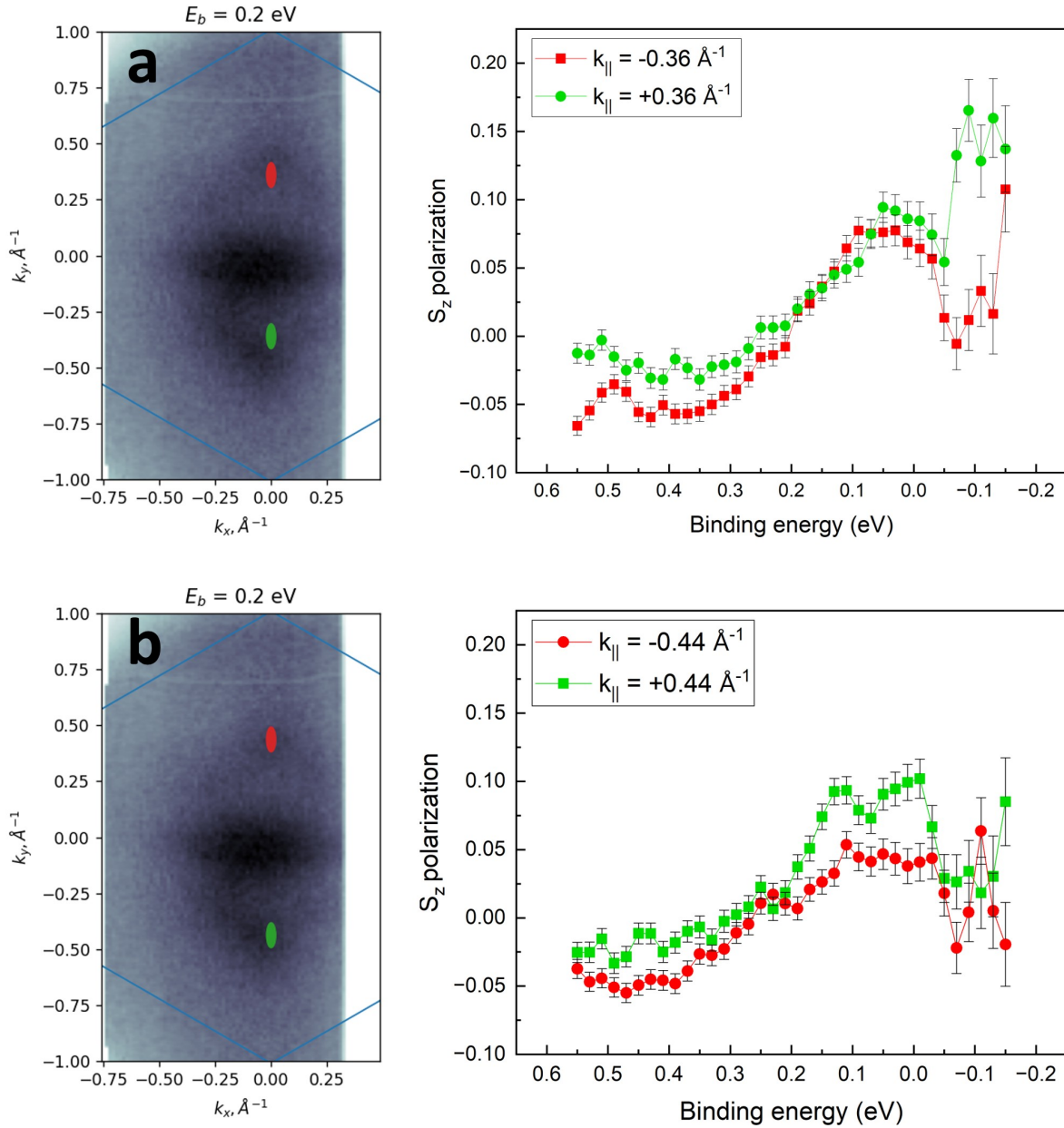


FIG. 10. SARPES data in more detail: spin-resolved EDCs and their angular position illustrated on iso-energy cuts at $E_B = 0.2 \text{ eV}$. Patches (red and green) illustrate angular integration windows parallel and perpendicular to the HSA slits.

-
- [1] Libor Šmejkal, Jairo Sinova, and Tomas Jungwirth. Beyond conventional ferromagnetism and antiferromagnetism: A phase with nonrelativistic spin and crystal rotation symmetry. *Physical Review X*, 12(3):031042, 2022.
- [2] Libor Šmejkal, Jairo Sinova, and Tomas Jungwirth. Emerging research landscape of altermagnetism. *Physical Review X*, 12(4):040501, 2022.
- [3] Tomas Jungwirth, Jairo Sinova, Rafael M Fernandes, Qihang Liu, Hikaru Watanabe, Shuichi Murakami, Satoru Nakatsuji, and Libor Šmejkal. Symmetry, microscopy and spectroscopy signatures of altermagnetism. *Nature*, 649(8098):837–847, 2026.
- [4] OJ Amin, A Dal Din, E Golias, Y Niu, A Zakharov, SC Fromage, CJB Fields, SL Heywood, RB Cousins, F Maccherozzi, et al. Nanoscale imaging and control of altermagnetism in mnte. *Nature*, 636(8042):348–353, 2024.
- [5] Mark E Schlesinger. The mn-te (manganese-tellurium) system. *Journal of phase equilibria*, 19(6):591–596, 1998.
- [6] Deepti Jain, Hee Taek Yi, Alessandro R Mazza, Kim Kisslinger, Myung-Geun Han, Matthew Brahlek, and Seongshik Oh. Buffer-layer-controlled nickeline vs zinc-blende/wurtzite-type mnte growths on c-plane al 2 o 3 substrates. *Physical Review Materials*, 8(1):014203, 2024.
- [7] Juraž Krempaský, L Šmejkal, SW D’souza, M Hajlaoui, G Springholz, K Uhlířová, F Alarab, PC Constantinou, V Strocov, D Usanov, et al. Altermagnetic lifting of kramers spin degeneracy. *Nature*, 626(7999):517–522, 2024.
- [8] T Osumi, S Souma, T Aoyama, K Yamauchi, A Honma, K Nakayama, T Takahashi, Kenya Ohgushi, and Takafumi Sato. Observation of a giant band splitting in altermagnetic mnte. *Physical Review B*, 109(11):115102, 2024.
- [9] Suyoung Lee, Sangjae Lee, Saegyeol Jung, Jiwon Jung, Donghan Kim, Yeonjae Lee, Byeongjun Seok, Jaeyoung Kim, Byeong Gyu Park, Libor Šmejkal, et al. Broken kramers degeneracy in altermagnetic mnte. *Physical review letters*, 132(3):036702, 2024.
- [10] Mahdi Hajlaoui, Sunil Wilfred D’Souza, Libor Šmejkal, Dominik Kriegner, Gauthier Krizman, Tetiana Zakusylo, Natalia Olszowska, Ondřej Caha, Jan Michalička, Jaime Sánchez-Barriga, Alberto Marmodoro, Karel Výborný, Arthur Ernst, Mirko Cinchetti, Jan Minar, Tomas Jungwirth, and Gunther Springholz. Temperature dependence of relativistic valence band splitting

- induced by an altermagnetic phase transition. *Advanced Materials*, 36(31):2314076, 2024.
- [11] NN Orlova, VD Esin, AV Timonina, NN Kolesnikov, and EV Deviatov. Magnetization symmetry for the mnte altermagnetic candidate. *arXiv preprint arXiv:2502.11876*, 2025.
- [12] Nadezhda Nikolaevna Orlova, Artem Aleksandrovich Avakyants, Anna Vladimirovna Timonina, Nikolay Nikolaevich Kolesnikov, and EV Deviatov. Crossover from relativistic to non-relativistic net magnetization for mnte altermagnet candidate. *JETP Letters*, 120(5):360–366, 2024.
- [13] KD Belashchenko. Giant strain-induced spin splitting effect in mnte, ag-wave altermagnetic semiconductor. *Physical Review Letters*, 134(8):086701, 2025.
- [14] Ji-Eun Lee, Yong Zhong, Qile Li, Mark T Edmonds, Zhi-Xun Shen, Choongyu Hwang, and Sung-Kwan Mo. Dichotomous temperature response in the electronic structure of epitaxially grown altermagnet mnte. *Nano Letters*, 2025.
- [15] Davide Bossini, Marc Terschanski, Fabian Mertens, Gunther Springholz, Alberta Bonanni, Götz S Uhrig, and Mirko Cinchetti. Exchange-mediated magnetic blue-shift of the band-gap energy in the antiferromagnetic semiconductor mnte. *New Journal of Physics*, 22(8):083029, 2020.
- [16] Dominik Kriegner, K Vybornyĭ, K Olejník, H Reichlová, V Novák, X Marti, J Gazquez, V Saidl, P Němec, VV Volobuev, et al. Multiple-stable anisotropic magnetoresistance memory in antiferromagnetic mnte. *Nature communications*, 7(1):11623, 2016.
- [17] RD Gonzalez Betancourt, Jan Zubáč, R Gonzalez-Hernandez, Kevin Geishendorf, Zbynek Šobáň, Gunther Springholz, Kamil Olejník, Libor Šmejkal, Jairo Sinova, Tomas Jungwirth, et al. Spontaneous anomalous hall effect arising from an unconventional compensated magnetic phase in a semiconductor. *Physical Review Letters*, 130(3):036702, 2023.
- [18] A Hariki, A Dal Din, OJ Amin, T Yamaguchi, A Badura, D Kriegner, KW Edmonds, RP Champion, P Wadley, D Backes, et al. X-ray magnetic circular dichroism in altermagnetic α -mnte. *Physical Review Letters*, 132(17):176701, 2024.
- [19] D Takegami, T Aoyama, T Okauchi, T Yamaguchi, S Tippireddy, S Agrestini, M García-Fernández, T Mizokawa, K Ohgushi, Ke-Jin Zhou, et al. Circular dichroism in resonant inelastic x-ray scattering: Probing altermagnetic domains in mnte. *arXiv preprint arXiv:2502.10809*, 2025.
- [20] Peter Krüger. Circular dichroism in resonant photoelectron diffraction as a direct probe of

- sublattice magnetization in altermagnets. *arXiv preprint arXiv:2504.08380*, 2025.
- [21] SW Lovesey, DD Khalyavin, and G Van Der Laan. Templates for magnetic symmetry and altermagnetism in hexagonal mnte. *Physical Review B*, 108(17):174437, 2023.
- [22] A Hariki, T Okauchi, Y Takahashi, and J Kuneš. Determination of the néel vector in rutile altermagnets through x-ray magnetic circular dichroism: The case of mnf 2. *Physical Review B*, 110(10):L100402, 2024.
- [23] Libor Šmejkal, Allan H MacDonald, Jairo Sinova, Satoru Nakatsuji, and Tomas Jungwirth. Anomalous hall antiferromagnets. *Nature Reviews Materials*, 7(6):482–496, 2022.
- [24] Chiu-Yun Lin, Luca Moreschini, and Alessandra Lanzara. Present and future trends in spin arpes. *Europhysics Letters*, 134(5):57001, 2021.
- [25] Taichi Okuda. Recent trends in spin-resolved photoelectron spectroscopy. *Journal of Physics: Condensed Matter*, 29(48):483001, 2017.
- [26] J Hugo Dil. Spin-and angle-resolved photoemission on topological materials. *Electronic Structure*, 1(2):023001, 2019.
- [27] A Dal Din, DA Usanov, L Šmejkal, SW D’Souza, F Guo, OJ Amin, EM Dawa, RP Campion, KW Edmonds, B Kiraly, et al. Unconventional relativistic spin polarization of electronic bands in an altermagnet. *arXiv preprint arXiv:2511.01690*, 2025.
- [28] Simon Moser. An experimentalist’s guide to the matrix element in angle resolved photoemission. *Journal of Electron Spectroscopy and Related Phenomena*, 214:29–52, 2017.
- [29] Ulrich Heinzmann and J Hugo Dil. Spin–orbit-induced photoelectron spin polarization in angle-resolved photoemission from both atomic and condensed matter targets. *Journal of Physics: Condensed Matter*, 24(17):173001, 2012.
- [30] Fabian Meier, Vladimir Petrov, Hossein Mirhosseini, Luc Patthey, Jürgen Henk, Jürg Osterwalder, and J Hugo Dil. Interference of spin states in photoemission from sb/ag (111) surface alloys. *Journal of Physics: Condensed Matter*, 23(7):072207, 2011.
- [31] Mauro Fanciulli, Henrieta Volfová, Stefan Muff, Jürgen Braun, Hubert Ebert, Jan Minár, Ulrich Heinzmann, and J Hugo Dil. Spin polarization and attosecond time delay in photoemission from spin degenerate states of solids. *Physical review letters*, 118(6):067402, 2017.
- [32] Jonathon Mark Riley, F Mazzola, M Dendzik, M Michiardi, T Takayama, Lewis Bawden, C Granerød, Mats Leandersson, T Balasubramanian, M Hoesch, et al. Direct observation of spin-polarized bulk bands in an inversion-symmetric semiconductor. *Nature Physics*,

- 10(11):835–839, 2014.
- [33] Meng Zeng, Pengfei Liu, Ming-Yuan Zhu, Naifu Zheng, Xiang-Rui Liu, Yu-Peng Zhu, Tian-Hao Shao, Yu-Jie Hao, Xiao-Ming Ma, Gexing Qu, et al. Non-altermagnetic spin texture in mnte. *arXiv preprint arXiv:2511.02447*, 2025.
- [34] Suyoung Lee. *Investigations on the electronic structures of magnetic transition metal chalcogenides*. PhD thesis, Department of Physics and Astronomy, Graduate School, Seoul National University, 2024.
- [35] Kazi Golam Martuza, Yogendra Kumar, Hiroshi Yamaguchi, Shiv Kumar, Masashi Arita, Hitoshi Sato, Shin-ichiro Ideta, and Kenya Shimada. Itinerant and correlated nature of altermagnetic mnte single crystal studied by photoemission and inverse-photoemission spectroscopies. *Materials*, 18(13):3103, 2025.
- [36] Gerd Schönhense. Circular dichroism and spin polarization in photoemission from adsorbates and non-magnetic solids. *Physica Scripta*, 1990(T31):255–275, 1990.
- [37] Usanov Dmitrii. *Spin-resolved electron spectroscopy: towards new instrumentation and unconventional magnetism*. PhD thesis, EPFL, Lausanne, 2025.
- [38] D Kriegner, H Reichlova, J Grenzer, W Schmidt, E Ressouche, J Godinho, T Wagner, SY Martin, AB Shick, VV Volobuev, et al. Magnetic anisotropy in antiferromagnetic hexagonal mnte. *Physical Review B*, 96(21):214418, 2017.
- [39] Georg Kresse and Jürgen Furthmüller. Efficient iterative schemes for ab initio total-energy calculations using a plane-wave basis set. *Physical review B*, 54(16):11169, 1996.
- [40] John P Perdew, Kieron Burke, and Matthias Ernzerhof. Generalized gradient approximation made simple. *Physical review letters*, 77(18):3865, 1996.
- [41] JB Pendry. Theory of photoemission. *Surface Science*, 57(2):679–705, 1976.
- [42] JFL Hopkinson, JB Pendry, and DJ Titterton. Calculation of photoemission spectra for surfaces of solids. *Computer Physics Communications*, 19(1):69–92, 1980.
- [43] John Brian Pendry. Low-energy electron diffraction. In *Interaction of Atoms and Molecules with Solid Surfaces*, pages 201–211. Springer, 1974.
- [44] H Ebert et al. The munich spr-kkr package, 2012.
- [45] H Ebert, D Ködderitzsch, and J Minár. Calculating condensed matter properties using the kkr-green’s function method—recent developments and applications. *Reports on Progress in Physics*, 74(9):096501, aug 2011.

- [46] AX Gray, C Papp, Shigenori Ueda, B Balke, Y Yamashita, L Plucinski, J Minár, J Braun, ER Ylvisaker, CM Schneider, et al. Probing bulk electronic structure with hard x-ray angle-resolved photoemission. *Nature materials*, 10(10):759–764, 2011.
- [47] G Malmström and J Rundgren. A program for calculation of the reflection and transmission of electrons through a surface potential barrier. *Computer Physics Communications*, 19(2):263–270, 1980.
- [48] J Braun. The theory of angle-resolved ultraviolet photoemission and its applications to ordered materials. *Reports on Progress in Physics*, 59(10):1267–1338, 1996.
- [49] Jürgen Braun, Ján Minár, and Hubert Ebert. Correlation, temperature and disorder: Recent developments in the one-step description of angle-resolved photoemission. *Physics Reports*, 740:1–34, 2018.
- [50] CM Polley, M Leandersson, J Adell, J Osiecki, D Carbone, K Ali, H Fedderwitz, and T Balasubramanian. The bloch beamline at max iv: Micro-spot arpes from a conventional, full-featured beamline. *Synchrotron Radiation News*, 37(4):18–23, 2024.
- [51] Franck Vidal, M Marangolo, P Torelli, M Eddrief, M Mulazzi, and G Panaccione. Circular dichroism in photoemission as a fingerprint of surface band structure: The case of znse (001)-c (2×2). *Physical Review B—Condensed Matter and Materials Physics*, 76(8):081302, 2007.